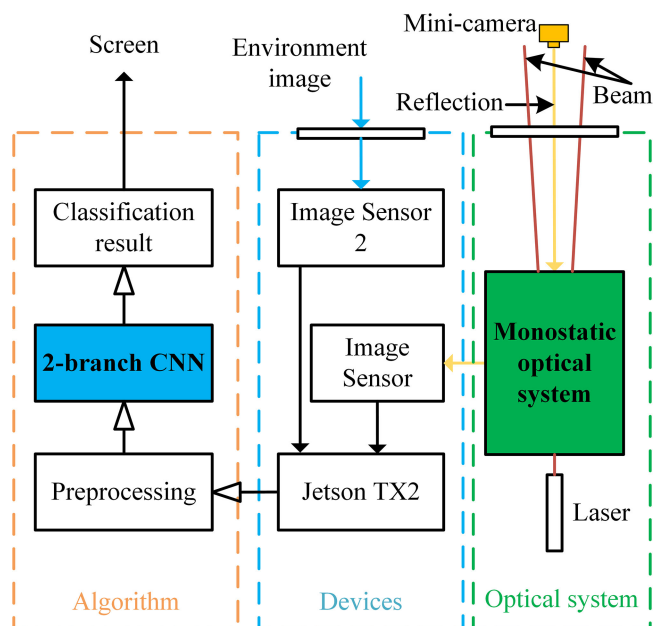


Design of an Active Laser Mini-Camera Detection System Using CNN



Volume 11, Number 6, December 2019

Chun Liu
Changming Zhao
Haiyang Zhang
Zilong Zhang
Yanwang Zhai
Yali Zhang



DOI: 10.1109/JPHOT.2019.2957521

Design of an Active Laser Mini-Camera Detection System Using CNN

Chun Liu , Changming Zhao, Haiyang Zhang , Zilong Zhang ,
Yanwang Zhai, and Yali Zhang

Beijing Institute of Technology, Beijing 100081, China

DOI:10.1109/JPHOT.2019.2957521

This work is licensed under a Creative Commons Attribution 4.0 License. For more information, see <https://creativecommons.org/licenses/by/4.0/>

Manuscript received October 19, 2019; revised November 19, 2019; accepted November 30, 2019. Date of publication December 4, 2019; date of current version December 17, 2019. Corresponding author: Haiyang Zhang (e-mail: ocean@bit.edu.cn).

Abstract: The growing popularity of the mini-camera is posing a serious threat to privacy and personal security. Disguised as common tools in rooms, these devices can become undetectable. Moreover, conventional active laser detection systems often fail to recognize them owing to their small lens size, weak reflectivity, and the influence of interference targets. In this paper, a method for building a laser active detection system for mini-cameras is proposed. Using a monostatic optical system and a deep learning classification algorithm, this anti-camera system can detect mini-cameras accurately in real time. This article describes the system components including its optical design, core components and image processing algorithm. The capability of the system for detecting mini-cameras and identifying interference is also experimentally demonstrated. This work successfully overcomes the limit of mini-camera detection using deep learning methods in active laser detection systems.

Index Terms: Mini-camera, active laser detection system, deep learning classification, interference target.

1. Introduction

In recent years, miniature photoelectric devices have been utilized for a wide range of applications. As one of the most common camera types, mini-cameras are typically characterized by their small size and can thus be deliberately hidden or disguised in rooms for illicit video recording. This is a serious threat to privacy and information security.

Traditional active laser detection systems utilize the chatoyancy effect, in which the laser beam is reflected directly back to the laser source by hidden camera lenses and the power of this retro-reflection is significantly higher than that of the diffuse background signal [1]–[4]. However, when detecting mini-cameras, there are several limitations: (1) The size of the lens aperture of a mini-camera is so small that the reflection is too weak to stand in stark contrast with the background; (2) the tiny lens aperture gives rise to a diffraction effect that further spreads the energy; and (3) reflective objects or other light sources can influence the system and can be incorrectly identified as the target cameras. These limitations bring about a critical reduction of reflection energy and inevitable false negative (FN) and false positive (FP) alerts.

Therefore, it is necessary to design a mini-camera detection system (MDS) based on the reflection of mini-cameras. Recent studies have investigated the chatoyancy effect for mini-camera devices. Long *et al.* [5] analyzed the diffraction phenomenon of the retro-reflection, whereas Change *et al.* [6] and Gong *et al.* [7] described the arrayed spots in reflected image profiles.

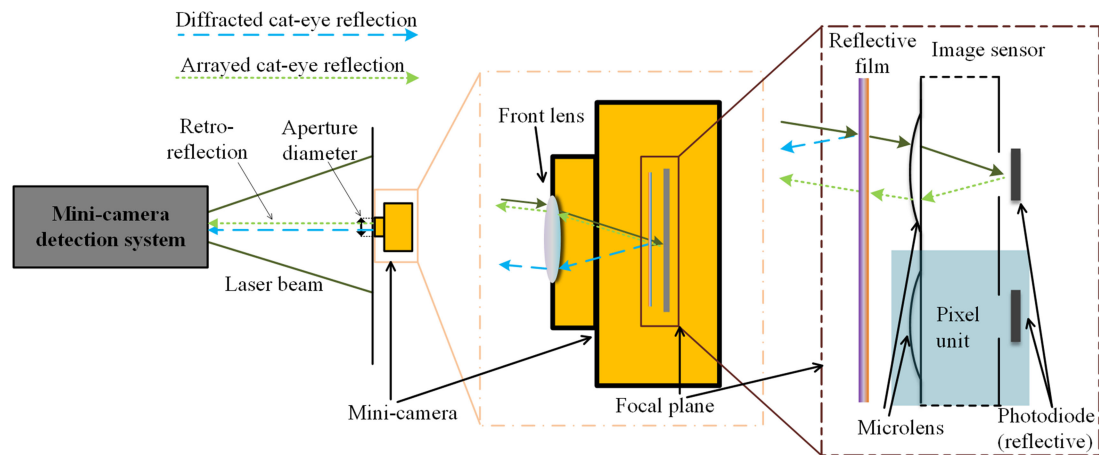


Fig. 1. Illustration of the detection process of a MDS and structure of a mini-camera.

Liu *et al.* [8] performed systematic analysis of mini-camera reflection, proposed an optical model, and implemented a reflection simulation. Based on these studies, this paper proposes an innovative method for building an anti-mini-camera system with a monostatic optical design and a convolutional neural network (CNN)-based classification algorithm. The monostatic optical system and the laser device ensure efficient reception of the mini-camera reflection. Additionally, the image algorithm uses preprocessing and CNN classification to determine whether the current image presents the mini-camera's reflection. Experimental results indicate that the MDS is capable of identifying typical mini-cameras and interference targets in real time. This work greatly improves the reflection image quality and recognition accuracy of mini-cameras using a particular optical design and deep learning. Thus, it fills gaps in the field of engineering active laser MDSs.

2. System Design

2.1 Principles of MDS

The principle of an MDS is shown in Fig. 1. When the diverging laser beam reaches the front lens of the mini-camera, only a small part of the beam can pass through its tiny lens aperture and enter the optical system. With regards to the beam, a portion of the light is reflected at the reflective film in front of the image sensor, and when it passes through the front lens again, diffraction occurs, leading to diffracted cat-eye reflection (DCR). The other portion of the beam that passes over the film will enter the image sensor, where the array-distributing micro lens and photodiode structures lead to a secondary chatoyancy effect, causing arrayed cat-eye reflection (ACR). Both reflected beams will propagate along the direction of the incident beam; however, their principles are different and thus, the light field distribution and their dependence on detection conditions will be quite different. In conventional research, the aperture of a cat-eye target is always large enough, or the detection distance is sufficiently far, that DCR will degenerate into traditional chatoyancy and become the main component of the reflection. In such situations, the shape of the reflection profiles will become a simple round spot. However, when detecting a mini-camera target under indoor conditions, the extremely weak ACR and DCR will be the only available retro-reflections, and their intensities will change as the defocus amount of the mini-camera varies. These characteristics explain the previously mentioned limitations when detecting mini-cameras using traditional laser active detection systems. Additionally, the reflection characteristics of mini-cameras under laser irradiation have been described and analyzed in detail by Liu *et al.* in reference [8].

In order to overcome the difficulties in mini-camera detection, this study focuses on the optical system and the design of an algorithm to address the issues of weak signals and classification.

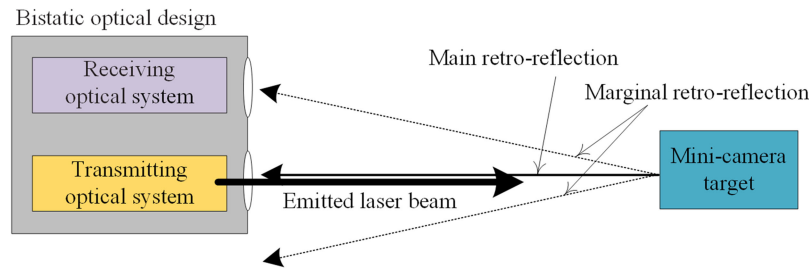


Fig. 2. Schematic demonstrating the problems of the bistatic optical design.

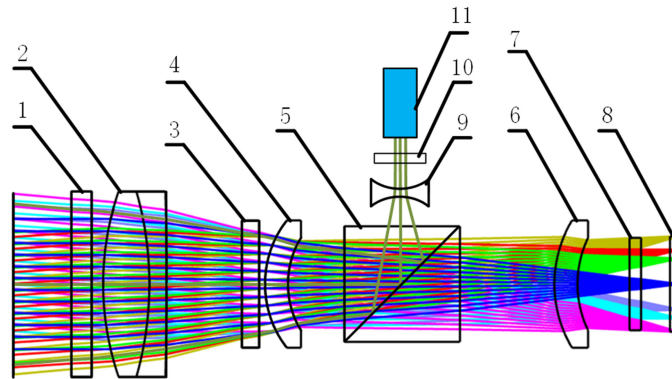


Fig. 3. Diagram of the monostatic optical system structure. 1. Plane mirror; 2. glued convex lens; 3. quarter-wave plate; 4, 6. convex lens; 5. polarization splitting prism; 7,10. polarizer; 8. narrow-band optical filter; 9. concave lens; and 11. laser device.

2.2 Optical System Design

In general, traditional cat-eye target detection systems are developed based on bistatic optical designs [4], [9], [10], where the transmitting and receiving optical axes are separated. These systems perform well when detecting larger, traditional cat-eye targets, but do not perform well when detecting mini-cameras. In the optical design shown in Fig. 2, the received echo signal will be extremely weak due to the following reasons: (1) the separation of the transmitting and receiving optical axes disrupts the normal incidence for detecting the laser reflection from the mini-camera; and (2) a detailed profile of the reflected image cannot be observed because a main part of the reflection occurs only along the transmitting optical axis, which is the path of the emitting laser. Moreover, the bistatic system occupies more space and is not convenient for production design.

To address these problems, we propose a monostatic optical system in which the transmitting optical path and receiving optical path share the same optical axis. This enables capturing of all or most reflection profiles and enhancement of the reflection signal. The only disadvantage of the monostatic design is that the optical system generates optical noise caused by inevitable beam reflection from the lens or polarizer. However, this problem can be solved by the preprocessing algorithm. At the system initialization stage, the system records the received image without any external input signals as a background image that contains most of the optical noise. Subsequently, we subtract the saved background image from the received images with external signals as inputs during preprocessing to reduce or even eliminate the effects of optical noise.

A schematic of the structure of the monostatic optical system is shown in Fig. 3. As for the transmitting optical path, the emitted laser beam will diverge at a certain angle. The laser beam is emitted from the semiconductor laser (component 11) and diverges after passing through components 10, 9, 5, 4, 3, 2, 1, respectively. The receiving optical path begins from the reflected

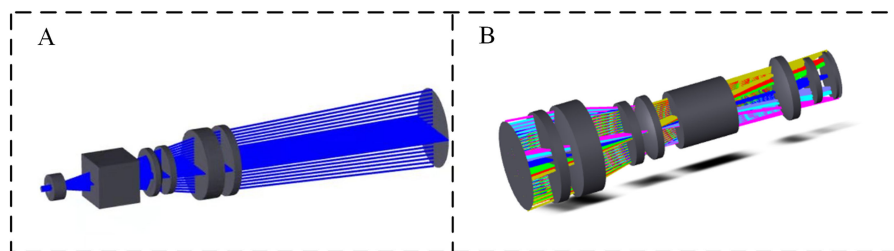


Fig. 4. Simulation of the optical path for (A) transmission path imaging and (B) laser beam receiving path.

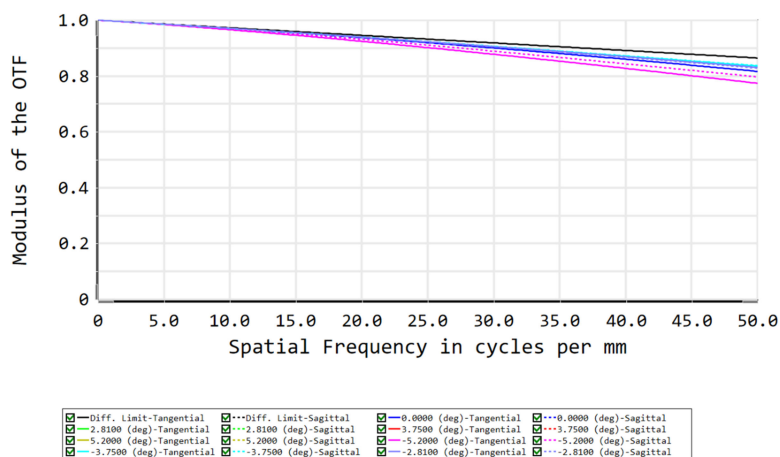


Fig. 5. Modulation transfer function analysis of the optical system. OTF signifies optical transfer function.

laser beam and passes through components 1 to 8. The reflected profile will finally be imaged on the sensor (to the right of 8). The receiving optical path shares an axis and components (1 to 5) with the transmitting optical path.

The laser beam transmission and receiving channels were both simulated using Zemax optical design software. The transmission channel simulation is shown in Fig. 4(A). The total length of the transmission channel is 86.855 mm. After passing through the optical system, the detection laser beam diverges by 10.4° , achieving a balance between detection efficiency and energy density of the detection laser beam. The laser beam receiving channel is shown in Fig. 4(B).

The modulation transfer function (MTF) of the optical system is shown in Fig. 5. The modulus of the optical transfer function (OTF) is above 0.8 at a spatial frequency of 50 lp/mm, indicating that the resolution and the imaging quality remain in good condition at a high spatial frequency.

To compare the effects of the bistatic and monostatic optical designs, we conducted a set of comparative experiments using a micro-imaging device with a 3.0 mm aperture front lens at a detection distance of 1.0 m. The reflection images from bistatic and monostatic designs are shown in Fig. 6(A) and (B), respectively.

Clearly, the bistatic optical system lost most of the signal, which is displayed as the diffraction rings shown in the monostatic optical system image. Only a bright spot can be observed in the bistatic optical system image. Although this sole bright spot feature can be recognized by some algorithms, it is undoubtedly far more difficult to distinguish than the rings observed in the monostatic images. Moreover, the monostatic system always has the potential to obtain normal-incident reflection images, which is beneficial for improving imaging quality.

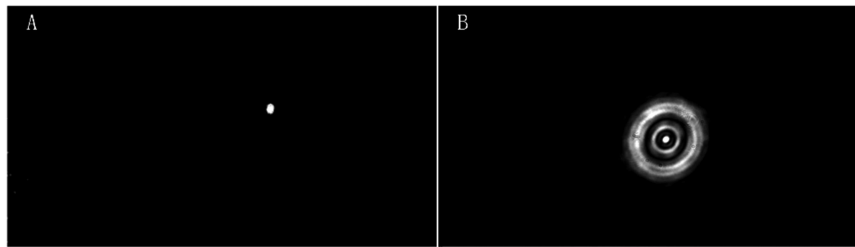


Fig. 6. Comparison of received beam profiles from (A) a bistatic and (B) a monostatic optical system.

TABLE 1
Main Components in an MDS and Their Key Parameters

Device	Key parameter	Remarks
Image sensor	Minimum Illuminance = 0.0001 lux Sensor size = 1"	High sensitivity will ensure reception of the weak reflected beam profile. Larger sensor size can expand the reception area.
Image sensor for environment	Field of view = 54°	Ensure that sufficient environmental information is acquired.
Laser source	Output power = 10.0 mW	Ensure that the reflection power is enough to be recognized but not so high as to be harmful to human eyes.
Embedded platform	RAM = 8 GB	This will be helpful for real-time performance.

2.3 Key Devices in the MDS

To ensure that the system operates effectively, in our experience, several key pieces of equipment must have sufficient performance. Some of the crucial parameters for major components are listed in Table 1. These parameters were utilized in this project and can be used as a reference. If a new MDS is designed, the parameters of the new system should be close to these values or at least not significantly lower.

2.4 Structure of the MDS

The general active laser MDS was built with the optical system, laser, and CMOS components on an embedded platform. The scheme is shown in Fig. 7(A). Image sensor 2 captures the pictures from the environment, which helps to determine the target location. Fig. 7(B) shows the MDS in the actual work environment where a keyboard, mouse, and screen are connected to the MDS for system control and interface display.

3. Algorithm Design

3.1 Reflection Image Classification

Traditional image classification methods may use texture features, local shape features and support vector machine (SVM) methods to implement image classification. In this project, it was found to be impractically difficult to find suitable features to describe all true target reflection images and all non-cat-eye target reflection images. Even if the proper descriptors were designed, the algorithm would be quite time consuming, hindering the real-time performance. Further, the SVM method is limited by large-dataset training, which may not simultaneously take each reflection type into account, thereby limiting the accuracy of the system.

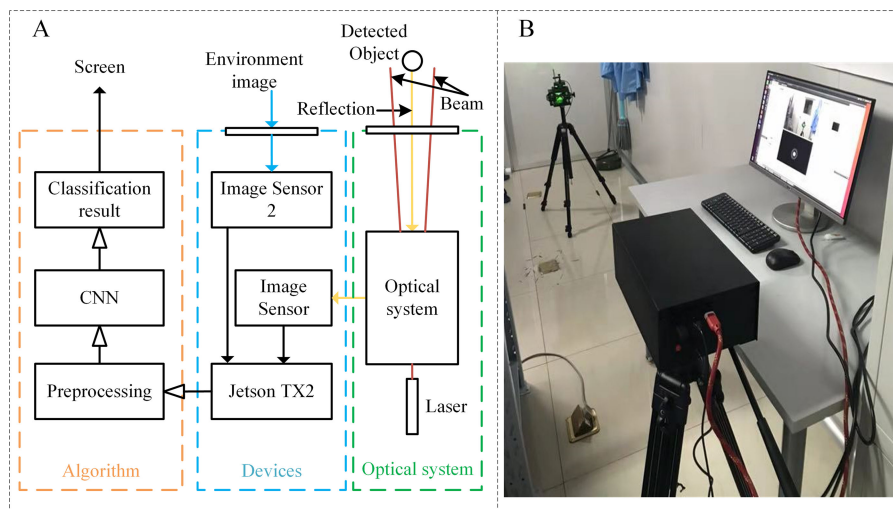


Fig. 7. (A) Schematic diagram. (B) System set-up of the mini-camera detection system (MDS).

In recent years, deep learning algorithms such as CNNs have shown good performance with regard to classification tasks [11]–[16]. Therefore, a lightweight CNN is adopted in our proposed MDS to detect mini camera devices in real time.

Depending on the optical system, the embedded system acquires a large number of reflection images that will be organized into two classes: (1) reflection images received when detecting various targets under various conditions; and (2) all possible reflection images received without any targets present in the detection area.

The reflection images of targets are divided into four main types; diffraction, array, traditional cat-eye, and mixed [8] as shown in Fig. 8.

Non-target images also have several main forms obtained under the following conditions: (1) no obvious reflection in the detection area; (2) object reflection at short distances; (3) objects such as plastic bottles and metals with reflective surfaces; and (4) other light sources irradiating the system.

3.2 Image Processing Algorithm

As the system needs to recognize targets immediately, it is necessary to implement high-accuracy real-time calculations in the embedded AI device.

The algorithms, including preprocessing and CNN, are specifically designed for mini-camera detection work. The following algorithms are designed for particular purposes, as explained below:

- 1) In the background difference method, the initial image, without external reflections, will be set as the background image. All subsequent images, when detecting targets, will perform differential operations with the recorded background image. This will essentially eliminate optical noise from the lens reflection in the monostatic optical system.
- 2) The image-gaining method will equally increase the gray value of image pixels. This process will address the weak reflection signal problem that occurs with mini-camera devices and causes difficulty in recognition.
- 3) With a large dataset including various mini-camera reflection images and non-target reflection image samples, the CNN classification algorithm can greatly improve the recognition accuracy and reduce interference image misclassification.

After preprocessing the optimized images become the input of the CNN classification algorithm. The network structure design adopts a lightweight structure suitable for the embedded system. The overall algorithm flowchart is shown in Fig. 10.

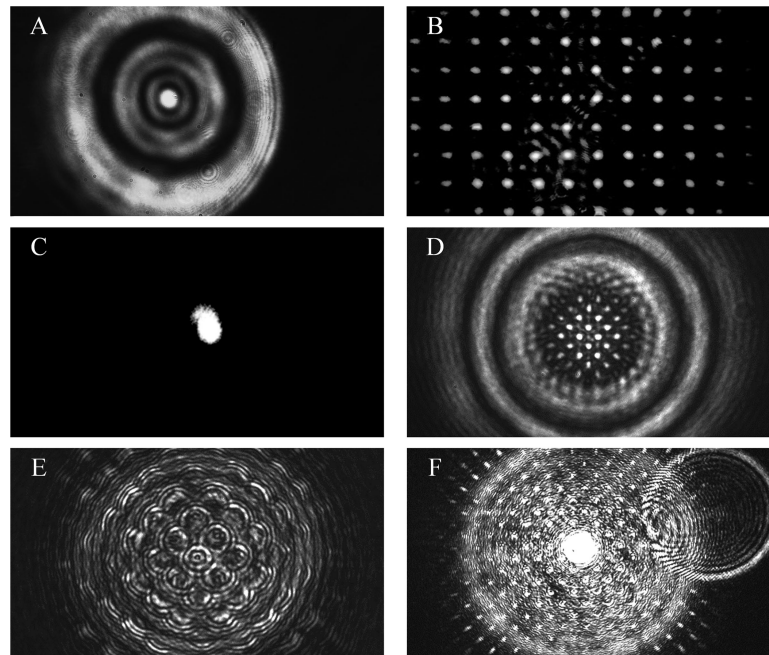


Fig. 8. Primary types of target reflection images. (A) Diffraction, (B) array, (C) traditional cat-eye, (D–F) mixed.

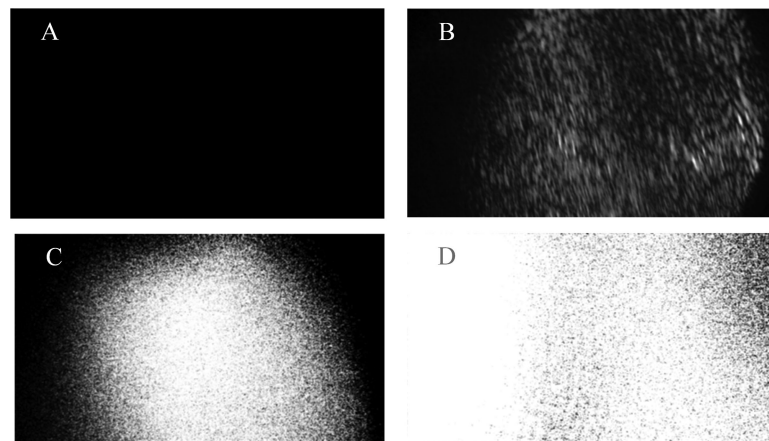


Fig. 9. Main forms of non-target reflection images under conditions with (A) no obvious reflection, (B) object reflection at short distances, (C) objects with reflective surfaces, and (D) other light sources.

Preprocessing operations include background difference, image gaining, and region of interest (ROI) selection. The background difference method is explained in detail by Li *et al.* [17]. Image gaining is a digital image processing method that increases the gray value of an image. The CNN was trained on a PC and uploaded to the Jetson TX2, which is a high-performance embedded platform. To avoid an output close to 0.5, which would be an intermediate state and make it difficult to determine the classification result, we subtracted the output from a threshold value and multiplied the difference by a certain coefficient, thereby increasing the dispersion degree of the classification result and making it close to either 0.0 or 0.999. In this project, the threshold value was set at 0.75 and the coefficient value was 4, which were informed by practical experience. Under these

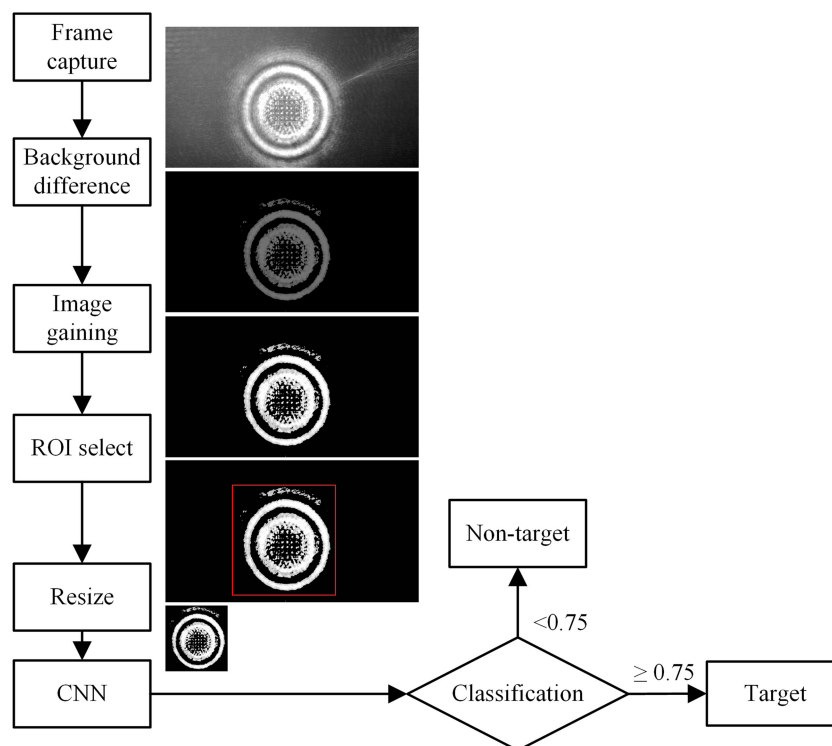


Fig. 10. MDS image processing algorithm. ROI and CNN denote region of interest and convolutional neural network, respectively.

conditions, the system worked well and was more likely to avoid misjudgment, especially false positive errors.

With the final percentage value F indicating the possibility of a true target being detected and the output of the neural network denoted as P , the post processing steps applied to the CNN output value can be expressed as

$$F = 100 \cdot \delta [P + 4 \cdot (P - 0.75)], \quad (1)$$

where δ represents the range protection function, and the result values exceeding $[0, 99.9]$ are set as the boundary values.

As for the CNN, a two-branch CNN structure was designed to classify the complex profiles in real time; this structure is inspired by the idea of GoogLeNet [18]. As shown in Fig. 11, after two large-kernel convolution layers, the two branches are separated. The first branch is designed for DCR features. In this branch the convolutional layers with 5×5 kernel size are used to ensure a large receptive field. This greatly improves the ability to distinguish the DCR profiles and the interference targets (otherwise, the interference target reflection images that have stripe-shape profiles would be recognized as the target reflection). Another branch uses more channels, while the kernel size of the convolution layer is set to 3×3 . The depth of both branches is limited to six to ensure speedy calculations. A parametric rectified linear unit (PReLU) activation function was selected to increase the penalty when the output is negative. This enhanced the negative outputs in each layer and thus improved the ability to identify interference targets. After convolution and pooling operations, two fully connected layers are implemented to connect the output feature maps from the two branches.

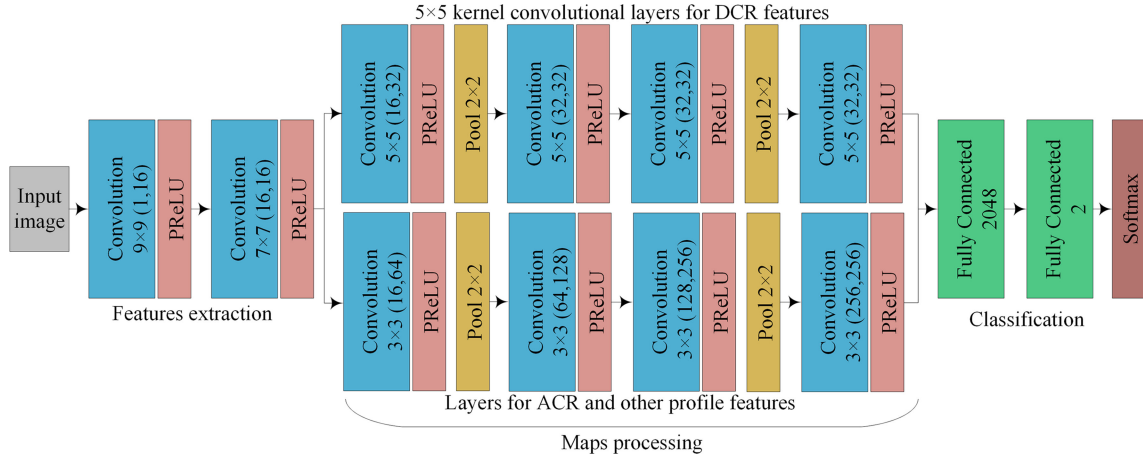


Fig. 11. Schematic diagram of the two-branch CNN architecture.

TABLE 2
Training Parameters

Parameter	Input tensor size	Epoch	Optimizer	Initial learning rate	Dataset (before data augmentation)
Value	[10, 1, 256, 256]	80	Adam	0.001	Target: 4000 Non-target: 4800

The feature maps of layer l are represented by tensors x^l , and the relationship with the previous layer x^{l-1} is presented as

$$x^l = \text{PReLU}(w^l * x^{l-1} + b^l), \quad (2)$$

where w^l denotes the weight matrix, b^l represents the offset vector, and $*$ denotes the convolution. After the last fully connected layer, the output nodes are placed into the softmax function and the result indicates the following probability:

$$\hat{y}_i |_{x,w,b} = \text{softmax}_i(w * x + b) = \frac{e^{z_i}}{\sum_j e^{z_j}}, \quad (3)$$

where $i = 1, 2$ and $z_i = (w * x + b)_i$.

The network is trained by the Adam optimizer algorithm with m samples, and the loss function is defined as the cross entropy of the classification result. Thus,

$$J = -\frac{1}{m} \sum_{k=1}^m \left[y_1^{(k)} \log(\hat{y}_1^{(k)}) + y_2^{(k)} \log(\hat{y}_2^{(k)}) \right] + \alpha \sum_{l=1}^L \|w^l\|_1, \quad (4)$$

where $\hat{y}_1^{(k)}$ represents the estimated possibility that the k -th sample image is a target reflection and $y_1^{(k)}$ takes the value 0 or 1, representing the real state of this sample. $\hat{y}_2^{(k)}$ and $y_2^{(k)}$ are corresponded to the non-target situations. The L1 regularization term is adopted to prevent overfitting. The training parameters are shown in Table 2. The pictures in the dataset are captured by the MDS, as described in Section 3.1.

4. Experimental Verification

The experiments were conducted in a laboratory environment. Real targets and non-cat-eye targets were fixed in front of the MDS. The incident angle was controlled within 1° , so that all types of

TABLE 3
Experimental Conditions

Environment	illumination	Detection distance	Incident angle	Mini-camera front aperture (diameter)	Normal-size front aperture (diameter)
Office	100 lux	0.55–3.0 m	$<1.0^\circ$	1.0–2.4 mm	>6.4 mm

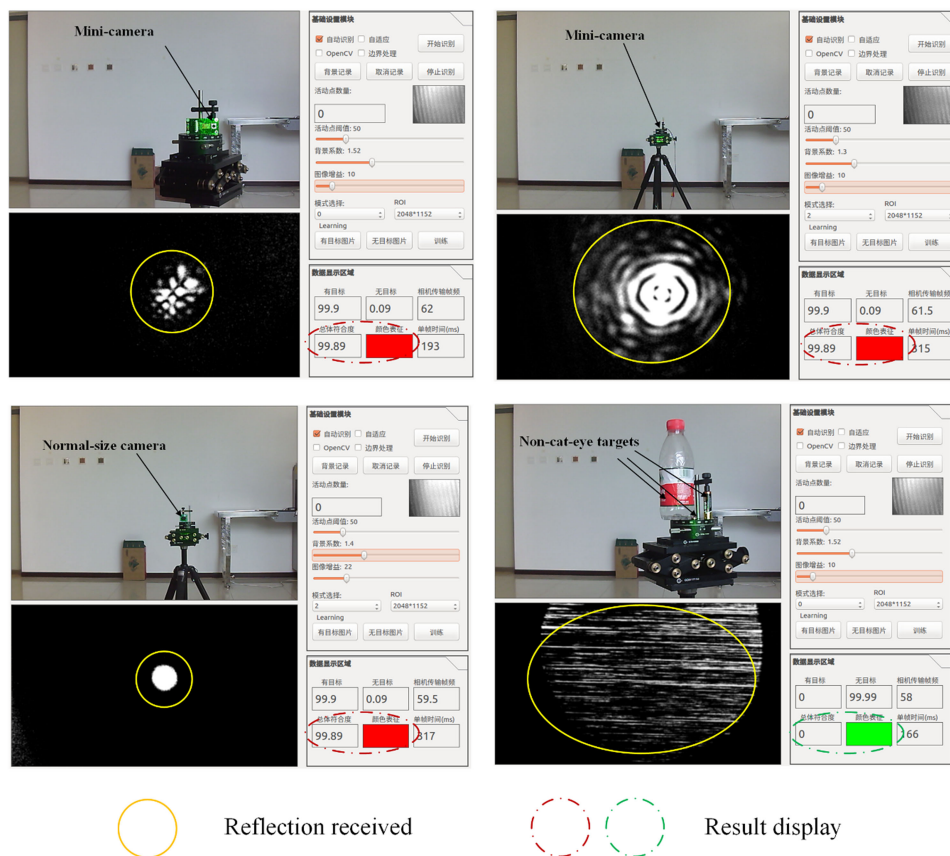


Fig. 12. Experimental results for different detection targets. (Red indicates targets and green indicates non-cat-eye targets).

reflections from mini-camera targets could be easily acquired. When the incident angle increases, the reflection profile gradually deforms and the energy weakens, making the recognition more uncertain. Table 3 lists the main parameters related to the experiments.

Screenshots of experimental results are shown in in Fig. 12, indicating that the MDS made correct judgments for each of the tested targets.

We performed 2000 sets of experiments for the detection system to recognize targets. Different mini-cameras were set as the detected objects in 500 recognition attempts, while in another 500 recognition attempts, different traditional-sized-camera targets were placed instead for recognition. Interference targets such as plastic bottles and batteries were posed as the detected objects in the last 1000 recognition attempts. Comparative experiments using the detection system with the following changes were then performed:

- 1) The background difference method (BDM) and image-gaining method (IGM) preprocessing were cancelled (Modification method A).

TABLE 4
Experimental Results for Different and Modified Detection Systems

Results	Method proposed in this work	Modification method A	Modification method B	Modification method C	Bistatic detection system
Normal-size camera	476/500	383/500	432/500	464/500	397/500
Mini-camera	466/500	372/500	327/500	391/500	285/500
Interference targets	976/1000	924/1000	980/1000	892/1000	671/1000
Recall (%)	94.20	75.50	75.90	85.50	68.20
Accuracy (%)	95.90	83.95	86.95	87.35	67.65

- 2) The laser emission power was reduced by half (Modification method B).
- 3) The CNN architecture was replaced by a traditional 1-branch CNN, the 5×5 kernel branch was removed (Modification method C).

Finally, a traditional bistatic cat-eye target detection system was utilized to perform an extra set of experiments to compare the optical systems. It had the same parameters as the proposed monostatic system. The results are summarized in Table 4. The numbers in the table represent the number of times the system correctly recognized the target out of 500 or 1000 attempts.

According to these results, the method proposed in this work achieved the best accuracy, compared with the modified methods. The results indicate that the BDM and IGM made significant contributions to the true positive (TP) results for all target types. Emission power is important for the quality of the target's reflection image, thus affecting the mini-camera recognition TP results. The two-branch CNN architecture performed better than the traditional CNN without the 5×5 kernel branch, especially for mini-camera and interference targets classification. Moreover, the traditional bistatic detection system has a poor capability for detecting mini-cameras and recognizing interference targets. The results indicate that the devices and algorithms of the MDS proposed in this paper make an important contribution to detection systems.

5. Conclusion

Mini-cameras pose many hidden dangers for personal privacy and security in important places. Their small lens size and weak reflection upon laser-irradiation make it difficult for traditional cat-eye detection equipment to capture them. In this paper, a mini-camera detection system (MDS) based on a monostatic optical design was proposed. The complete reflection beam profile can be obtained with this optical design. In the embedded platform, an efficient preprocessing algorithm and a CNN image classification algorithm are employed to realize detection and identification. The preprocessing algorithm eliminates the inter-lens reflection interference and amplifies the reflection image, and the CNN classification algorithm achieves high-accuracy target and non-target classification. Moreover, because all potential types of reflection images are collected in the training dataset, the trained network can identify various types of mini-cameras and interference targets effectively. The experimental results verify the detection capability of MDS for mini-cameras and interference targets. This system provides the highest accuracy for mini-camera detection to date.

The limitations of the proposed system is the range of detection distances and angles of incidence, because the reflection intensity of a mini-camera is greatly reduced with the degradation of these two conditions. The dependence of a traditional cat-eye target reflection on incident angle has been studied in [19], [20], while the mini-camera's distant or oblique-incidence reflection has been analyzed in [5], [8]. However, the actual upper limits of the distance and incident angle vary greatly depending on the working conditions and target characteristics of each system. We can empirically define them as 0–4.0 m and 0–5° for the system described in this article. These limits can be increased to a certain extent if the laser emission power is increased or if the quality of the image sensor is improved. If tremendous improvement is required, further breakthroughs in the system principles will be needed, which could lead to a new research field.

In terms of the algorithm, calculation speed could be increased by converting the traditional convolution process to pointwise group convolution and channel shuffle, which is referred to in the ShuffleNet [21]. In addition, optimizing tools such as TensorRT may further increase the speed of interference process.

The proposed MDS still has some potential to improve. However, the existing system has achieved ideal results when detecting mini-cameras with small incident angles in indoor scenes, and thus fills a gap in the field of active laser detection technology.

Acknowledgment

The authors would like to thank the anonymous reviewers for their valuable suggestions.

References

- [1] K. Qin, S. Han, and C. Zeng, "Analysis of active laser detection distance for 'cat's-eye' target," *Opt. Techn.*, vol. 35, pp. 486–488, 2009.
- [2] B. Zhou, B. Liu, and D. Wu, "Research on echo energy of 'cat-eye' target based on laser's character of polarization," in *Proc. Int. Conf. Electron. Optoelectron.*, Dalian, China, pp. 29–31, Jul. 2011.
- [3] X. Ren and L. Li, "Recognizing cat-eye targets with dual criterions of shape and modulation frequency," *Chin. Opt. Lett.*, vol. 9, 2011, doi: [10.3788/COL20110904.41101](https://doi.org/10.3788/COL20110904.41101).
- [4] D. Wu, T. Bai, B. Liu, B. Zhou, and W. Hu, "Dynamic imaging detection and target recognition for cat-eye effect echo," *Acta Optica Sinica*, vol. 33, pp. 87–92, 2013, doi: [10.3788/AOS201333.0811003](https://doi.org/10.3788/AOS201333.0811003).
- [5] M. Long, H. Zhang, and C. Liu, "Spatial modulation characteristics of micro-lens for irradiated laser," *Acta Optica Sinica*, vol. 37, 2017, doi: [0.3788/AOS201737.1205001](https://doi.org/0.3788/AOS201737.1205001).
- [6] C. Chang, M. Su, Y. Yang, and J. Tsai, "Design, fabrication, and characterization of tunable cat-eye retroreflector arrays as optical identification tags," *J. Lightw. Technol.*, vol. 32, no. 3, pp. 384–391, Feb. 2014.
- [7] M. Gong, S. He, R. Guo, and W. Wang, "Cat-eye effect reflected beam profiles of an optical system with sensor array," *Appl. Opt.*, vol. 55, pp. 4461–4466, 2016.
- [8] C. Liu, C. Zhao, H. Zhang, Z. Zhang, S. Gao, and Y. Wang, "Analysis of mini-camera's cat-eye retro-reflection for characterization of diffraction rings and arrayed spots," *IEEE Photon. J.*, vol. 11, no. 4, Aug. 2019, Art. no. 6802412.
- [9] M. Gong and S. He, "Periodicity analysis on cat-eye reflected beam profiles of optical detectors," *Opt. Eng.* vol. 56, 2017, Art. no. 053110, doi: [10.1117/1.OE.56.5.053110](https://doi.org/10.1117/1.OE.56.5.053110).
- [10] L. Li, J. Ren, and X. Wang, "Fast cat-eye effect target recognition based on saliency extraction," *Opt. Commun.*, vol. 350, pp. 33–39, 2015.
- [11] G. Liang, H. Hong, W. Xie, and L. Zheng, "Combining convolutional neural network with recursive neural network for blood cell image classification," *IEEE Access*, vol. 6, pp. 36188–36197, 2018, doi: [10.1109/ACCESS.2018.2846685](https://doi.org/10.1109/ACCESS.2018.2846685).
- [12] Y. Liu, C. Suen, Y. Liu, and L. Ding, "Scene classification using hierarchical Wasserstein CNN," *IEEE Trans. Geosci. Remote Sens.*, vol. 57, no. 5, pp. 2494–2509, May 2019.
- [13] J. Jiang, X. Feng, F. Liu, Y. Xu, and H. Huang, "Multi-spectral RGB-NIR image classification using double-channel CNN," *IEEE Access*, vol. 7, pp. 20607–20613, 2019, doi: [10.1109/ACCESS.2019.2896128](https://doi.org/10.1109/ACCESS.2019.2896128).
- [14] A. Krizhevsky, I. Sutskever, and G. E. Hinton, "ImageNet classification with deep convolutional neural networks," *Adv. Neural Inf. Process. Syst.*, vol. 25, pp. 1097–1105, 2012, doi: [10.1145/3065386](https://doi.org/10.1145/3065386).
- [15] I. Amerini, C. Li, and R. Caldelli, "Social network identification through image classification with CNN," *IEEE Access*, vol. 7, pp. 35264–35273, 2019, doi: [10.1109/ACCESS.2019.2903876](https://doi.org/10.1109/ACCESS.2019.2903876).
- [16] M. Han, R. Cong, X. Li, H. Fu, and J. Lei, "Joint spatial-spectral hyperspectral image classification based on convolutional neural network," *Pattern Recognit. Lett.*, vol. 20, pp. 15, 2018, doi: [10.1016/j.patrec.2018.10.003](https://doi.org/10.1016/j.patrec.2018.10.003).
- [17] L. Li, H. Li, E. Dang, and B. Liu, "Compressive sensing method for recognizing cat-eye effect targets," *Appl. Opt.*, vol. 52, pp. 7033–7039, 2013, doi: [10.1364/AO.52.007033](https://doi.org/10.1364/AO.52.007033).
- [18] C. Szegedy *et al.*, "Going deeper with convolutions," in *Proc. IEEE Conf. Comput. Vis. Pattern Recognit.*, 2015, pp. 1–9, doi: [10.1109/CVPR.2015.7298594](https://doi.org/10.1109/CVPR.2015.7298594).
- [19] Y. Zhao, H. Sun, L. Zhang, and Y. Zheng, "Light intensity at the return place and encirclement power ratio for the distorted reflected beam based on cat-eye effect," *Optoelectron. Lett.*, vol. 7, no. 6, pp. 0478–0482, 2011, doi: [10.1007/s11801-011-1055-2](https://doi.org/10.1007/s11801-011-1055-2).
- [20] Y. Zhao, H. Sun, L. Zhang, and Y. Zheng, "Backwards propagation characteristics of distorted reflected beams with cat-eye effect," *Chin. J. Lasers*, vol. 38, no. 7, 2011, doi: [10.3788/CJL201138.0702015](https://doi.org/10.3788/CJL201138.0702015).
- [21] X. Zhang, X. Zhou, M. Lin, J. Sun, "ShuffleNet: An extremely efficient convolutional neural network for mobile devices," *Conf. Comput. Vision and Pattern Recognit.*, 2018, doi: [10.1109/cvpr.2018.00716](https://doi.org/10.1109/cvpr.2018.00716).